Strong evidence for couplings between the ionospheric wave-4 structure and atmospheric tides

Maosheng He,[1,2] Libo Liu,[1] Weixing Wan,[1] and Yong Wei[3]

Received 19 April 2011; revised 29 May 2011; accepted 31 May 2011; published 16 July 2011.

[1] Recently a so-called "wave-4 structure" was discovered in the equatorial ionosphere, which describes plasma density enhancements within four longitude sectors separated about 90° from each other. This structure was proposed to be controlled by the tide mode of DE3 (diurnal eastward-propagating with zonal wave number-3) excited by different heating in the tropical troposphere due to land-sea differences. Here, using F_2-layer peak density ($NmF2$) and the peak height ($hmF2$) extracted from the COSMIC data set, we investigate the wave-4 structure by decomposing it into interhemispheric symmetric and antisymmetric components. Our results indicate that the generally accepted mechanism of DE3 modulation of *E* region dynamo only accounts for the daytime symmetric components, while the antisymmetric components could be explained well in the terms of the SE2 (semidiurnal eastward-propagating with zonal wave number-2) tide in transequatorial neutral wind. Surprisingly, the antisymmetric component dominates the wave-4 structure in $hmF2$ during nighttime, suggesting the SE2 transequatorial wind is the leading contributor to the nighttime wave-4 structure in $hmF2$. **Citation:** He, M., L. Liu, W. Wan, and Y. Wei (2011), Strong evidence for couplings between the ionospheric wave-4 structure and atmospheric tides, *Geophys. Res. Lett.*, *38*, L14101, doi:10.1029/2011GL047855.

1. Introduction

[2] Longitudinal variations of the plasma density in the ionosphere are usually attributed to the differences in geomagnetic field configuration [*West and Heelis*, 1996; *He et al.*, 2009, 2011]. However, recent studies suggest that longitudinal wavelike structures in the equatorial ionosphere are controlled by atmospheric tides [e.g., *Sagawa et al.*, 2005]. Atmospheric tides refer to global-scale oscillations in the atmosphere with periods of integral fractions of a day. Among the non-sun-synchronous tidal components, the DE3 component is generally the most dynamical in the mesosphere/low thermosphere (MLT) region during most of the year [e.g., *Hagan and Forbes*, 2002; *Pedatella et al.*, 2008]. In a sun-synchronous frame, four longitudinal peaks are observed from the DE3 tide due to the Doppler Effect, known as wave-4 structure. The DE3 tide or wave-4 structure is widely observed in various neutral parameters in the MLT region, such as temperature and zonal winds [*Forbes et al.*, 2003, 2006].

[3] In the ionosphere, the wave-4 signature was first detected in the nighttime airglow intensity over equator, and was attributed to the DE3 modulation of the *E* region dynamo and *F* region fountain [*Sagawa et al.*, 2005; *Immel et al.*, 2006]. Evidence supporting this hypothesis includes the longitudinal wave-4 fluctuation in the vertical plasma drift and the spatiotemporal correlations between ionospheric wave-4 signatures and the DE3 tides in the MLT region [*Ren et al.*, 2009; *Wan et al.*, 2008, 2010]. However, recently it was argued that thermal tides could directly penetrate into the *F* region [*Forbes et al.*, 2009; *Häusler and Lühr*, 2009; *Oberheide et al.*, 2009, 2011; *Talaat and Lieberman*, 2010]. Numerical simulations [*England et al.*, 2010; *Zhang et al.*, 2010] also suggested that, in addition to the electrodynamic couplings, the penetration of tides into the *F* region could contribute directly to the ionospheric wave-4 structure. One purpose of the present work is to explore evidence for the electrodynamic coupling and the ionospheric signatures of direct penetration of tides to evaluate the contributions from the main processes.

[4] We also aim to explore the ionospheric wave-4 signatures from tides beyond the DE3. As illustrated in Figure 1, the wave-4 structure could arise from other tide modes besides the DE3, such as the DW5 (diurnal westward-propagating with zonal wave number-5), SPW4 (stationary planetary wave number-4), and SE2 (semidiurnal eastward wave number-2). An indicator supporting the connection between wave-4 structure and DE3 tide is that the wave-4 pattern shifts eastward at ~90°/day [e.g., *Wan et al.*, 2008; *Häusler and Lühr*, 2009; *Lühr et al.*, 2008]. However, the wave-4 pattern is found to be almost stationary in GUVI-O/N_2 [*He et al.*, 2010], suggesting a potential connection to the SPW4 mode. Based on an empirical model extended from tides in the MLT region, *Oberheide et al.* [2011] suggested that the ionospheric wave-4 structure was also contributed by the SE2 transequatorial wind resulted from tropospheric forcing and by the SPW4 and SE2 zonal winds excited by the nonlinear interaction between the DE3 and DW1 tides. Here, we report direct evidence in ionospheric wave-4 structures indicating considerable contributions from the SE2 tide mode.

2. Data and Methods

[5] The receivers on board COSMIC mission collected GPS signals, from which vertical electron density profiles were retrieved through the Radio Occultation technique. The COSMIC mission had collected more than 2.7 million profiles from May, 1, 2006 to November 29, 2010. This

[1]Beijing National Observatory of Space Environment, Institute of Geology and Geophysics, Chinese Academy of Sciences, Beijing, China.
[2]College of Earth Science, Graduate University of Chinese Academy of Sciences, Beijing, China.
[3]Max-Planck-Institut für Sonnensystemforschung, Katlenburg-Lindau, Germany.

Copyright 2011 by the American Geophysical Union.
0094-8276/11/2011GL047855

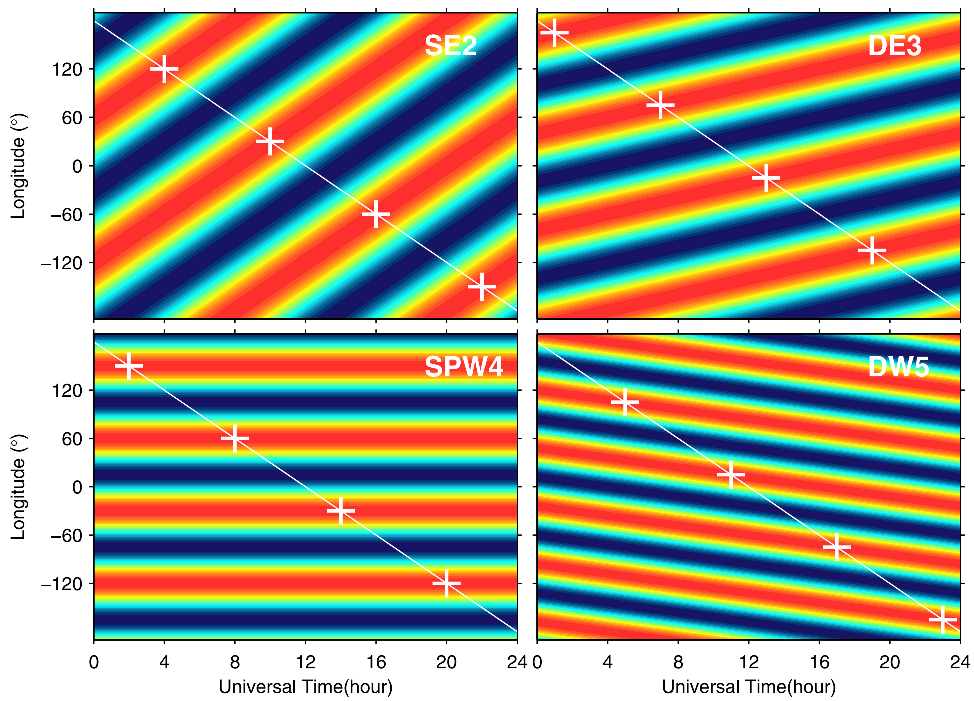

Figure 1. Sketch maps for four tide modes contributing potentially to the longitudinal wave-4 structure. The solid line in each panel indicates the isoline of 12 local time (*LT*). Pluses on each of the lines illustrate that four longitudinal peaks would be recorded in fixed *LT* frame as observed by (quasi-) Sun-synchronous satellites.

period corresponds to the minimum phase of solar cycle 23/24, during which the daily 10.7 cm solar radio flux (*F*10.7) varies from 65.1 to 103.2 ($10^{-22}\cdot\mathrm{Wm}^{-2}\cdot\mathrm{Hz}^{-1}$) with an average of 73.4. The level-2 products of COSMIC profiles are derived from the COSMIC Data Analysis and Archive Center. We fit each profile using a cubic spline to determine the F_2-layer peak density (*NmF*2) and its height (*hmF*2). To simplify data operations, we construct empirical models for *NmF*2, *hmF*2 via the following procedures.

[6] First, we pick up the data collected under geomagnetically quiet time (*Kp* index < 3) and then bin the *NmF*2 measurements by day of year (*DoY*) and geomagnetic longitude (*MLON*) with a resolution of 30.4 days by 15° longitudes (12 × 24 bins in total). In each *DoY-MLON* bin, we fit the coefficients (c_{mn}, c'_{mn}, s_{mn}, s'_{mn} (n = 0, 1…, 13, m = 1, 2…, n)) of the associated Legendre polynomials according to:

$$NmF2(MLAT, MLT, F10.7) = \sum_{m,n} P_n^m(\cos(MLAT)) \cdot [C_{mn}\cdot\cos(360^*MLT/24) + S_{mn}\cdot\sin(360^*MLT/24)],$$

where *MLAT* is geomagnetic latitude, *MLT* is the magnetic local time, P_n^m is the Legendre polynomial of degree n and order m, $C_{mn} = c_{mn} + c'_{mn}\cdot F10.7$ and $S_{mn} = s_{mn} + s'_{mn}\cdot F10.7$ are linear functions of *F*10.7. Second, in each *DoY-MLON* bin, *NmF*2 is computed by summing the Legendre polynomials on the 91 × 48 mesh grid of *MLAT* = −90, −88… 90 versus *MLT* = 0.25, 0.75… 23.75, at *F*10.7 = 70. Thus, *NmF*2 is represented by a 4-D matrix (12 × 24 × 91 × 48). Third, by separating variables into two groups, ⟨*DoY*, *MLON*⟩ and ⟨*MLAT*, *MLT*⟩, we reshape the 4-D matrix into a 2-D matrix (288 × 4368). Following the methodology introduced by *Jolliffe* [2002], we perform a Principal Components Analysis on the 2-D matrix, and construct the empirical model of *NmF*2 with four input parameters (*DoY*, *MLON*, *MLAT*, *MLT*) by summing the least principal components containing 99% variance of the total. Finally, following the similar procedures, we construct the empirical model of *hmF*2.

3. Results and Conclusions

[7] With the *NmF*2 model, we are able to calculate a series of the F_2-layer maximum electron density ($NmF2_i$) at a geomagnetic longitude series ($MLON_i = 15(i-1)$, i = 1, 2…24), at any *MLAT*, *LT* and *DoY*. Fourier analysis could be performed for the $NmF2_i$ according to the equation:

$$A_{Wn} = \frac{p}{24}\cdot\sum_{k=1}^{24} NmF2_k\cdot\omega^{(k-1)\cdot n}, n = 0, 1\ldots 11,$$

where $p = \begin{cases} 1, n = 0 \\ 2, n > 0 \end{cases}$, $\omega = e^{2\pi i/24}$, $i = \sqrt{-1}$. The calculated A_{W0} is the longitudinal average of *NmF*2 and $\boldsymbol{A_{W4}}$ is the wave number-4 component. We calculate the A_{W0} and $\boldsymbol{A_{W4}}$ on the mesh grid of *MLAT* = −30, −27.5… 30 versus *LT* = 0, 1… 24 at *DoY* 280, shown in Figure 2a. In Figure 2a, during 10—18 *LT* the ionization trough is created over the geomagnetic equator and the ionization anomaly crests around ±15°. The equatorial anomaly arises from the fountain effect: the *E* region dynamo electric field maps into the equatorial *F* region, causes **E** × **B** drift, and drives the plasma to great heights from where the plasma diffuses downward along field lines to subequatorial latitudes enhancing the subequatorial plasma density [*Hanson and Moffett*, 1966; *Immel et al.*, 2006]. Another striking feature in Figure 2a is the interhemispheric asymmetry of $\boldsymbol{A_{W4}}$,

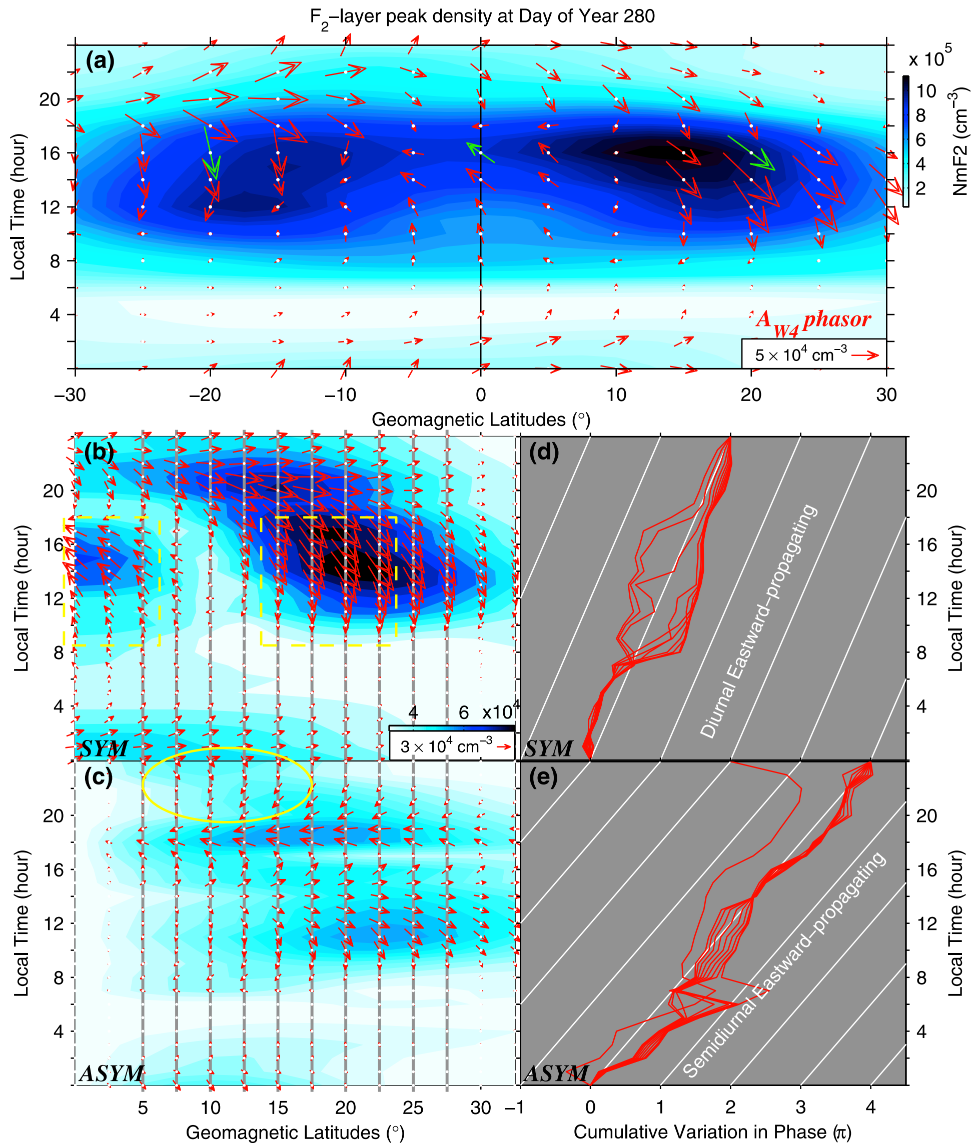

Figure 2. (a) Longitudinal average of *NmF*2 as a function of *MLAT* and *LT* at *DoY* 280, calculated from the COSMIC model described in the "Data and Methods" section. Arrows exhibit the Fourier-filtered phasor (also called phase vector or complex amplitude of the longitudinal wave-4 component $\boldsymbol{A_{W4}}$. The length of the arrow denotes the $\boldsymbol{A_{W4}}$ magnitude and the direction denotes the $\boldsymbol{A_{W4}}$ phase. For example, the rightward arrow stands for the $\boldsymbol{A_{W4}}$ component peaks at the four longitudes of 0° + n × 90° (n = 0, 1, 2, 3), the upward for 22.5° + n × 90°, and the leftward for 45° + n × 90°. (b) Phasor (arrow) and its magnitude (color code) of the interhemispheric symmetric wave-4 component $\boldsymbol{SYM_{W4}}$. (d) The diurnal cumulative variation in phase of the arrow on each of the gray lines in Figure 2b. Each red line in Figure 2d corresponds to a gray line in Figure 2b. (c, e) The same plots as Figures 2b and 2d but for the antisymmetric component $\boldsymbol{ASYM_{W4}}$. Dashed boxes in Figure 2b indicate that the $\boldsymbol{SYM_{W4}}$ at the equator is in antiphase with that at subequatorial latitudes. The arrows in the oval in Figure 2c would be compared with the corresponding arrows in Figure 3.

e.g., the magnitude of $\boldsymbol{A_{W4}}$ phasor peaks at 20° *MLAT*, 14 *LT* in the Northern Hemisphere but at 15° *MLAT*, 18 *LT* in the Southern. Figure 3a exhibits the same plot as Figure 2a but for *hmF*2, in which two bulges locate respectively around noon due to daytime maximum upward drift [*Fejer et al.*, 1991] and around the sunset due to pre-reversal enhancement [*Fejer et al.*, 1989]. The interhemispheric asymmetry of $\boldsymbol{A_{W4}}$ in Figure 3a is more significant. Particularly, at 00 *LT* the $\boldsymbol{A_{W4}}$ phasor at the northern subequatorial latitudes is opposite in phase to that at the southern, marked by the green arrows.

[8] In order to evaluate the asymmetries, we decompose the $\boldsymbol{A_{W4}}$ phasor in Figure 3a into interhemispheric symmetric and antisymmetric components ($\boldsymbol{SYM_{W4}}$ and $\boldsymbol{ASYM_{W4}}$, shown in Figures 3b and 3c, respectively):

$$\begin{cases} \boldsymbol{SYM}_{W4}(MLAT) = (\boldsymbol{A}_{W4}(MLAT) + \boldsymbol{A}_{W4}(-1 \cdot MLAT))/2 \\ \boldsymbol{ASYM}_{W4}(MLAT) = (\boldsymbol{A}_{W4}(MLAT) - \boldsymbol{A}_{W4}(-1 \cdot MLAT))/2 \end{cases}.$$

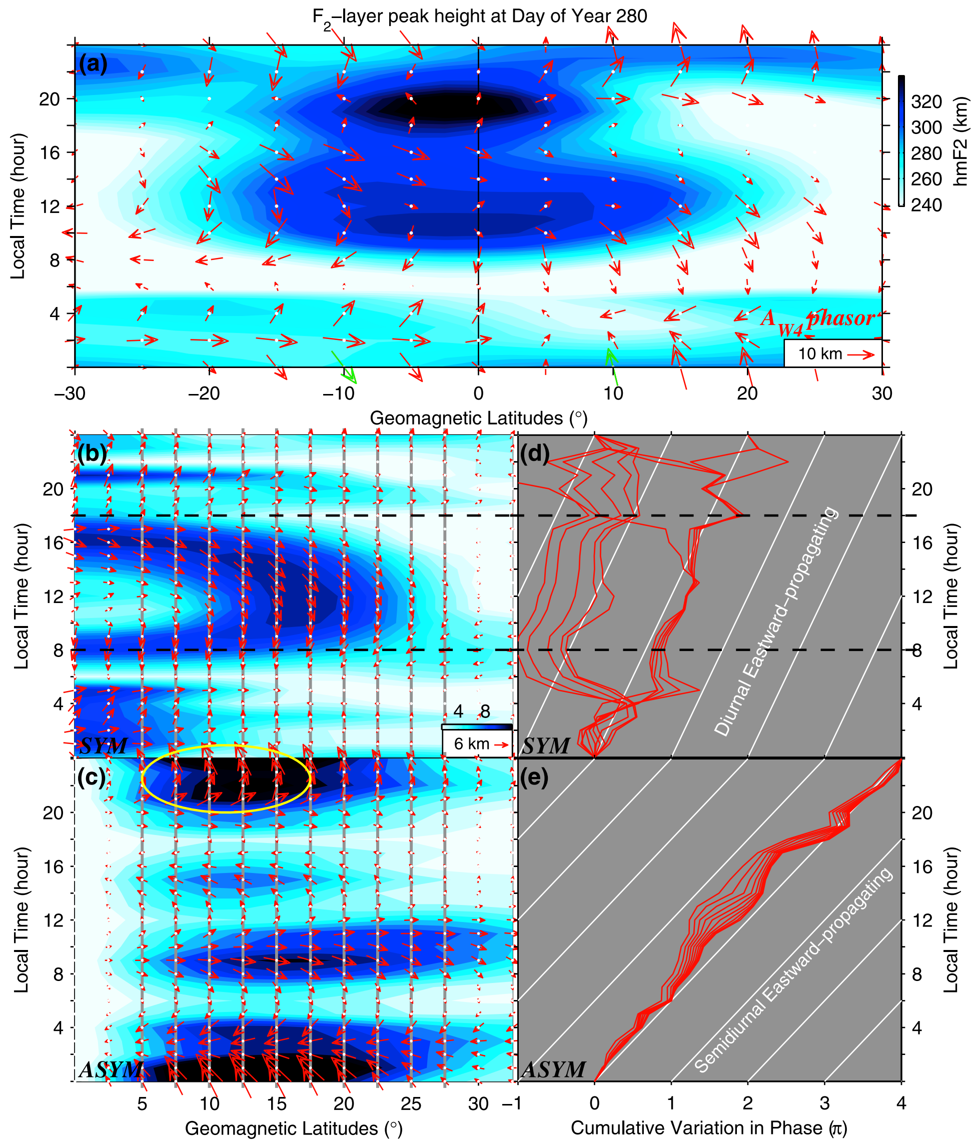

Figure 3. The same plot as Figure 2 but for *hmF*2. The $\boldsymbol{ASYM_{W4}}$ arrows in the oval in Figure 3c are largely opposite in phase to the corresponding *NmF*2 arrows in Figure 2c.

To quantify the phase variation with *LT*, we calculate the diurnal cumulative variation in the $\boldsymbol{SYM_{W4}}$ phase ($c\Phi$, shown in Figure 3d) along each gray line in Figure 3b:

$$c\Phi(LT_j) = \sum_{i=1}^{j} \delta\phi(LT_i),$$

where

$$\delta\phi(LT_i) = \begin{cases} 0, LT_i = 0 \\ \mathrm{Arg}(\boldsymbol{SYM}_{W4}(LT_i)/\boldsymbol{SYM}_{W4}(LT_{i-1})), LT_i = 1, 2 \ldots 24 \end{cases}.$$

During 08—18 *LT*, the $\boldsymbol{SYM_{W4}}$ phase increases at the rate of ~2π/day (Figure 3d), i.e., the rate of an eastward diurnal tide. Different from the $\boldsymbol{SYM_{W4}}$ component, the $\boldsymbol{ASYM_{W4}}$ phase increases at the rate of ~4π/day (Figure 3e). Similarly, we decompose the *NmF*2 $\boldsymbol{A_{W4}}$ phasor in Figure 2a into $\boldsymbol{SYM_{W4}}$ and $\boldsymbol{ASYM_{W4}}$, shown in Figures 2b and 2c. Generally, the $\boldsymbol{SYM_{W4}}$ phase increases at the rate of ~2π/day (Figure 2d) and the $\boldsymbol{ASYM_{W4}}$ at ~4π/day (Figure 2e), similar to those of *hmF*2. Among all tide modes contributing potentially to the wave-4 structure, only the DE3 mode propagates eastward at 2π/day and the SE2 at 4π/day. Thus, it is the SE2 and DE3 modes that account mainly for the $\boldsymbol{ASYM_{W4}}$ components and the daytime $\boldsymbol{SYM_{W4}}$ components, respectively.

[9] A simple consideration for the $\boldsymbol{ASYM_{W4}}$ components is with a SE2 tide in transequatorial neutral wind. The transequatorial wind transports plasma along the geomagnetic field lines, upwards (downward) in the upwind (downwind) hemisphere. Thus, the transport raises the F_2-layer peak at the upwind side but lowers it at the downwind side [*Rishbeth*, 2000], resulting in an interhemispheric asymmetry in *hmF*2. Contrary to the asymmetry in *hmF*2, in *NmF*2 an asymmetry would be produced with higher value at the downwind side [*Rishbeth*, 1977, 2000]. A fact supporting this supposition is that the *hmF*2 $\boldsymbol{ASYM_{W4}}$ is largely in antiphase with the *NmF*2 $\boldsymbol{ASYM_{W4}}$ at the subequatorial latitudes (arrows in the ovals in Figures 2c

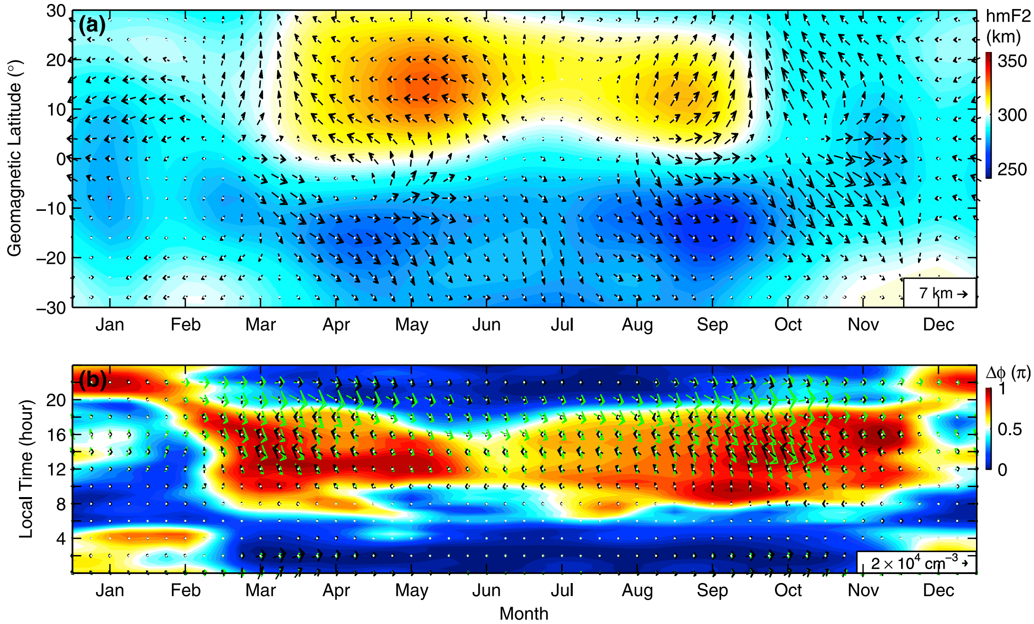

Figure 4. (a) Longitudinally average *hmF*2 (color code) at 00 *LT* as a function of month and *MLAT*, with the $\boldsymbol{A_{W4}}$ phasor (arrow) in *hmF*2. The interhemispheric asymmetry in the $\boldsymbol{A_{W4}}$ is significant. (b) *NmF*2 $\boldsymbol{SYM_{W4}}$ phasor at the equator (blank arrow) and 20° latitude (green arrow) as a function of month and *LT*, with the angle (color code) between the green and blank arrows.

and 3c). Besides, in Figure 3c, the $\boldsymbol{ASYM_{W4}}$ in *hmF*2 is generally stronger during nighttime than daytime, potentially arising from the less ion drag during nighttime for lower plasma density. The presence of the SE2 transequatorial wind in the *F* region is supported by the Hough mode extension empirical model [*Oberheide et al.*, 2011]. According to the modeling, long-wavelength SE2 tides excited in troposphere could penetrate into the *F* region, causing transequatorial SE2 winds with amplitude in excess of 10 m/s.

[10] The $\boldsymbol{SYM_{W4}}$ in *NmF*2 could be attributed to the DE3 modulation of the *E* region dynamo and the *F* region fountain [*Immel et al.*, 2006; *Sagawa et al.*, 2005]. A fact supporting this proposition is marked by the green arrows in Figure 2a. At 16 *LT*, the $\boldsymbol{A_{W4}}$ phasor over the northern crest is almost opposite in phase to that over the equator. At the longitude where the dynamo electric field is enhanced most by the DE3 tide, the upward drift would be enhanced most, and so does the drainage of plasma from the equatorial region to subequatorial latitudes, resulting in a zonal minimum plasma density over the equator accompanying with a zonal maximum at subequatorial latitudes. In Figure 2b, the antiphase between the $\boldsymbol{SYM_{W4}}$ over the equator and that at 15—25° *MLAT* persists just during daytime from 9 to 18 *LT*. After sunset, the plasma in the *E* region depletes quickly and the *E* region conductivity decreases considerably in the absence of solar irradiation, resulting in the disappearances of the *E* region dynamo and the associated wave-4 structures. Meanwhile, the daytime $\boldsymbol{SYM_{W4}}$ in *hmF*2 could also be attributed to the tidal modulation of the *E* region dynamo. The upward drift driven by the eastward electric field starts in the morning and reaches its diurnal maximum around the noon [*Fejer et al.*, 1991; *Scherliess and Fejer*, 1999]. An enhanced upward drift would transport the plasma to higher altitude to diffuse further poleward. Accordingly, the $\boldsymbol{SYM_{W4}}$ magnitude in Figure 3b exhibits a U-shaped pattern during daytime and peaks around noon.

[11] Generally, the *NmF*2 $\boldsymbol{A_{W4}}$ phasor in Figure 2a is dominated by the $\boldsymbol{SYM_{W4}}$ component while the *hmF*2 phasor in Figure 3a is dominated by the $\boldsymbol{ASYM_{W4}}$ component from 18 to 10 *LT*, which suggests the DE3 modulation on the electrodynamic coupling is the leading contributor to the wave-4 structure in *NmF*2 but the transequatorial SE2 wind is the major contributor to the nighttime wave-4 structure in *hmF*2.

[12] The main behaviors reported above at *DoY* 280 could be found during most of the year, observed from plots same as Figures 2 and 3 but for all other months (not shown). For example, around midnight the $\boldsymbol{A_{W4}}$ phasor at northern subequatorial latitudes is opposite in phase to that at the southern in most months (Figure 4a), and the daytime antiphase between the $\boldsymbol{SYM_{W4}}$ over the equator and $\boldsymbol{SYM_{W4}}$ at the subequatorial latitudes persists from March to November (Figure 4b).

[13] In summary, considerable interhemispheric asymmetries are observed in wave-4 structures of *NmF*2 and *hmF*2. In particular, around midnight nearly antiphase wave-4 component in *hmF*2 is observed at the equatorial flanks. The wave-4 structures in *NmF*2 and *hmF*2 are decomposed into interhemispheric symmetric and antisymmetric components ($\boldsymbol{SYM_{W4}}$ and $\boldsymbol{ASYM_{W4}}$). The $\boldsymbol{ASYM_{W4}}$ components in both *NmF*2 and *hmF*2 shift eastward at the rate of 4π/day while the $\boldsymbol{SYM_{W4}}$ components at the rate of 2π/day during daytime. The daytime $\boldsymbol{SYM_{W4}}$ components are attributed to the DE3 modulation of the *E* region dynamo, while the $\boldsymbol{ASYM_{W4}}$ components are attributed to a SE2 tide in transequatorial wind. Evidence supporting the above hypotheses includes: 1) The *NmF*2 $\boldsymbol{SYM_{W4}}$ at the equator is in antiphase to that at the 15—25° during daytime, indicating the draining and diffusing effects of the

fountain. 2) During daytime, the *hmF*2 $\boldsymbol{SYM_{W4}}$ enhances within a U-shape pattern, which could be ascribed to the daytime variation of eastward electric field and the associated upward drift. 3) At the subequatorial latitudes, the *hmF*2 $\boldsymbol{ASYM_{W4}}$ is largely opposite in phase to the *NmF*2 $\boldsymbol{ASYM_{W4}}$, which could be explained in the terms of SE2 tide in transequatorial wind.

[14] **Acknowledgments.** The authors thank Kazuo Shiokawa for his kindly help. This research is supported by National Natural Science Foundation of China (40725014, 41074112) and the China Meteorological Administration Grant (No. GYHY201106011). Y. Wei is supported by National Natural Science Foundation of China (41004072).

[15] The Editor thanks two anonymous reviewers for their assistance in evaluating this paper.

References

England, S. L., T. J. Immel, J. D. Huba, M. E. Hagan, A. Maute, and R. DeMajistre (2010), Modeling of multiple effects of atmospheric tides on the ionosphere: An examination of possible coupling mechanisms responsible for the longitudinal structure of the equatorial ionosphere, *J. Geophys. Res.*, *115*, A05308, doi:10.1029/2009JA014894.

Fejer, B. G., E. R. de Paula, I. S. Batista, E. Bonelli, and R. F. Woodman (1989), Equatorial F region vertical plasma drifts during solar maxima, *J. Geophys. Res.*, *94*(A9), 12,049–12,054, doi:10.1029/JA094iA09p12049.

Fejer, B. G., E. R. de Paula, S. A. González, and R. F. Woodman (1991), Average vertical and zonal F region plasma drifts over Jicamarca, *J. Geophys. Res.*, *96*(A8), 13,901–13,906, doi:10.1029/91JA01171.

Forbes, J. M., X. Zhang, E. R. Talaat, and W. Ward (2003), Nonmigrating diurnal tides in the thermosphere, *J. Geophys. Res.*, *108*(A1), 1033, doi:10.1029/2002JA009262.

Forbes, J. M., J. Russell, S. Miyahara, X. Zhang, S. Palo, M. Mlynczak, C. J. Mertens, and M. E. Hagan (2006), Troposphere-thermosphere tidal coupling as measured by the SABER instrument on TIMED during July–September 2002, *J. Geophys. Res.*, *111*, A10S06, doi:10.1029/2005JA011492.

Forbes, J. M., S. L. Bruinsma, X. Zhang, and J. Oberheide (2009), Surface-exosphere coupling due to thermal tides, *Geophys. Res. Lett.*, *36*, L15812, doi:10.1029/2009GL038748.

Hagan, M. E., and J. M. Forbes (2002), Migrating and nonmigrating diurnal tides in the middle and upper atmosphere excited by tropospheric latent heat release, *J. Geophys. Res.*, *107*(D24), 4754, doi:10.1029/2001JD001236.

Hanson, W. B., and R. J. Moffett (1966), Ionization transport effects in the equatorial F region, *J. Geophys. Res.*, *71*(23), 5559–5572, doi:10.1029/JZ071i023p05559.

Häusler, K., and H. Lühr (2009), Nonmigrating tidal signals in the upper thermospheric zonal wind at equatorial latitudes as observed by CHAMP, *Ann. Geophys.*, *27*, 2643–2652, doi:10.5194/angeo-27-2643-2009.

He, M., et al. (2009), A study of the Weddell Sea Anomaly observed by FORMOSAT-3/COSMIC, *J. Geophys. Res.*, *114*, A12309, doi:10.1029/2009JA014175.

He, M., L. Liu, W. Wan, J. Lei, and B. Zhao (2010), Longitudinal modulation of the O/N2 column density retrieved from TIMED/GUVI measurement, *Geophys. Res. Lett.*, *37*, L20108, doi:10.1029/2010GL045105.

He, M., L. Liu, W. Wan, and B. Zhao (2011), A study on the nighttime midlatitude ionospheric trough, *J. Geophys. Res.*, *116*, A05315, doi:10.1029/2010JA016252.

Immel, T. J., et al. (2006), Control of equatorial ionospheric morphology by atmospheric tides, *Geophys. Res. Lett.*, *33*, L15108, doi:10.1029/2006GL026161.

Jolliffe, I. T. (2002), *Principal Component Analysis*, 2nd ed., Springer-Verlag New York, Inc., New York.

Lühr, H., M. Rother, K. Häusler, P. Alken, and S. Maus (2008), The influence of nonmigrating tides on the longitudinal variation of the equatorial electrojet, *J. Geophys. Res.*, *113*, A08313, doi:10.1029/2008JA013064.

Oberheide, J., J. M. Forbes, K. Häusler, Q. Wu, and S. L. Bruinsma (2009), Tropospheric tides from 80 to 400 km: Propagation, interannual variability, and solar cycle effects, *J. Geophys. Res.*, *114*, D00I05, doi:10.1029/2009JD012388.

Oberheide, J., J. M. Forbes, X. Zhang, and S. L. Bruinsma (2011), Wave-driven variability in the ionosphere-thermosphere-mesosphere system from TIMED observations: What contributes to the "wave 4"?, *J. Geophys. Res.*, *116*, A01306, doi:10.1029/2010JA015911.

Pedatella, N. M., J. M. Forbes, and J. Oberheide (2008), Intra-annual variability of the low-latitude ionosphere due to nonmigrating tides, *Geophys. Res. Lett.*, *35*, L18104, doi:10.1029/2008GL035332.

Ren, Z., W. Wan, L. Liu, and J. Xiong (2009), Intra-annual variation of wave number 4 structure of vertical E × B drifts in the equatorial ionosphere seen from ROCSAT-1, *J. Geophys. Res.*, *114*, A05308, doi:10.1029/2009JA014060.

Rishbeth, H. (1977), Dynamics of the equatorial *F* region, *J. Atmos. Terr. Phys.*, *39*(9–10), 1159–1168, doi:10.1016/0021-9169(77)90024-1.

Rishbeth, H. (2000), The equatorial F-layer: Progress and puzzles, *Ann. Geophys.*, *18*(7), 730–739, doi:10.1007/s00585-000-0730-6.

Sagawa, E., T. J. Immel, H. U. Frey, and S. B. Mende (2005), Longitudinal structure of the equatorial anomaly in the nighttime ionosphere observed by IMAGE/FUV, *J. Geophys. Res.*, *110*, A11302, doi:10.1029/2004JA010848.

Scherliess, L., and B. G. Fejer (1999), Radar and satellite global equatorial F region vertical drift model, *J. Geophys. Res.*, *104*(A4), 6829–6842, doi:10.1029/1999JA900025.

Talaat, E. R., and R. S. Lieberman (2010), Direct observations of nonmigrating diurnal tides in the equatorial thermosphere, *Geophys. Res. Lett.*, *37*, L04803, doi:10.1029/2009GL041845.

Wan, W., et al. (2008), Wavenumber-4 patterns of the total electron content over the low latitude ionosphere, *Geophys. Res. Lett.*, *35*, L12104, doi:10.1029/2008GL033755.

Wan, W., et al. (2010), Correlation between the ionospheric WN4 signature and the upper atmospheric DE3 tide, *J. Geophys. Res.*, *115*, A11303, doi:10.1029/2010JA015527.

West, K. H., and R. A. Heelis (1996), Longitude variations in ion composition in the morning and evening topside equatorial ionosphere near solar minimum, *J. Geophys. Res.*, *101*(A4), 7951–7960, doi:10.1029/95JA03377.

Zhang, Y., S. England, and L. J. Paxton (2010), Thermospheric composition variations due to nonmigrating tides and their effect on ionosphere, *Geophys. Res. Lett.*, *37*, L17103, doi:10.1029/2010GL044313.

M. He, L. Liu, and W. Wan, Beijing National Observatory of Space Environment, Institute of Geology and Geophysics, Chinese Academy of Sciences, Beijing 100029, China. (hems@mail.igcas.ac.cn; liul@mail.iggcas.ac.cn; wanw@mail.iggcas.ac.cn)

Y. Wei, Max-Planck-Institut für Sonnensystemforschung, Katlenburg-Lindau, Germany. (wei@mps.mpg.de)